

Prospects for sub-EW ALP searches via $\gamma + b\bar{b}$ signatures at the LHC using jet substructure techniques

A. Adhikary,^a A. Bharucha,^a L. Feligioni^b and M. Frigerio^c

^a*Aix Marseille Univ, Université de Toulon, CNRS, CPT, IPhU, Marseille, France*

^b*Aix Marseille Univ, CNRS/IN2P3, CPPM, Marseille, France*

^c*Laboratoire Charles Coulomb (L2C), University of Montpellier and CNRS, Montpellier, France*

E-mail: amit.adhikary@cpt.univ-mrs.fr

ABSTRACT: The current Large Hadron Collider (LHC) data show no clear indication of new physics and only incremental improvements are anticipated at the energy frontier in the near future. However, while the focus of the LHC has been on constraining TeV scale physics, new particles could still be hiding below the electroweak scale. In order to obtain sensitivity to a new light boson with couplings to SM fermions, a potentially promising decay channel, for resonances with mass $\gtrsim \mathcal{O}(10)$ GeV, would be the decay to $b\bar{b}$ pairs. The measurement of such signatures is challenging due to the trigger requirements at the LHC. In this work, we explore the LHC sensitivity to a light pseudoscalar, or axion-like particle (ALP), in the $b\bar{b}$ final state with an associated photon, using jet substructure techniques, in the mass range between 10 GeV and 100 GeV. We obtain projected exclusions on the ALP-fermion coupling in a region of phase space which has not so far been probed by direct searches. We further discuss the impact that lower trigger thresholds may have on the LHC reach.

Contents

1	Introduction	1
2	Light pseudoscalar: model and motivations	4
3	Collider Analysis	5
3.1	Event simulation	6
3.2	Object definitions and event selection	6
3.3	Flavour labelling and b -tagging on the simulated events	10
3.4	Signal extraction and background estimation	14
4	Results	16
4.1	Projected sensitivities on the cross-section and coupling	16
4.2	Analysis with low p_T threshold	18
4.3	Interpretation of the results	18
5	Summary and outlook	20

1 Introduction

The excellent performance of the LHC in terms of delivered luminosity has allowed the ATLAS and CMS experiments to set stringent limits on new particle masses well beyond the electroweak (EW) scale, thus worsening the naturalness problem. However, it is still possible that the new physics is hidden at lower energies, being weakly coupled to the known Standard Model (SM) particles, such that any sign of its production are swamped by the SM background. Current resonance searches at the LHC leave an area of opportunity roughly below the EW scale, which could potentially be accessed via the $b\bar{b}$ final state. Light scalars and pseudoscalars are particularly promising candidates, with possibly large branching ratios to $b\bar{b}$ if their masses are above 10 GeV, as further discussed in Section 2. The resonances may be identified with well-motivated axion-like particles (ALPs) [1–5]. They could be mediators between the SM and dark matter (DM) [6–10]. Such spin-zero particles with masses below the EW scale could further arise in models such as the next-to-minimal supersymmetric SM [11], or composite Higgs models with additional Nambu-Goldstone bosons [12–16].

Previous searches targeting low mass hadronic resonances have been carried out by the ATLAS and CMS collaborations. From the experimental point of view, the challenge starts already at the trigger level, where stringent requirements on hadronic jets transverse momentum (p_T) are usually needed in order to cope with the bandwidth limitations of the LHC experiments data acquisition system. ATLAS searched for singly produced $q\bar{q}$

resolved resonances in 29.3 fb^{-1} of proton-proton collision at a center-of-mass energy $\sqrt{s} = 13 \text{ TeV}$, using Trigger Level Analysis [17] (TLA), a technique that allows to lower the trigger threshold by recording only the information calculated by the jet trigger algorithms in the High Level Trigger. Making use of a single jet trigger with a p_{T} threshold of 185 GeV, the TLA sets a limit on an axial-vector DM mediator with couplings to SM quarks and mass above 450 GeV.

The production of light resonances is often investigated via associate production with other particles, such as high energetic photons or quark and gluons from initial state radiation (ISR), less overwhelmed by the SM processes and consequently less challenging to trigger on, though presenting significantly smaller and possibly more model-dependent production rates. CMS searched for boosted light resonances decaying into collimated quark pairs, recoiling from high- p_{T} quark/gluon radiation, using a data sample of 41.1 fb^{-1} of proton-proton collision at a center-of-mass energy of $\sqrt{s} = 13 \text{ TeV}$ [18]. These resonances are looked for in single large radius jet, reconstructed with the anti- k_{T} clustering algorithm [19] of radius $R=0.8$ (AK8) and distinguished from the dominant QCD background by exploiting the jet substructure. For this search CMS uses a combination of triggers based on the scalar sum of the jet p_{T} s (H_{T}) and on leading jet p_{T} thresholds. The offline leading AK8 jet is required to have $p_{\text{T}} > 525 \text{ GeV}$, this condition ensures that the trigger is fully efficient with respect to the offline selection. By identifying the leading jet as produced by the resonance decay products, CMS is able to set a limit on lepto-phobic Z' with masses from 50 to 250 GeV. CMS also searched for low mass resonances as an excess arising in the invariant mass spectrum of two-pronged substructure within an AK8 jet recoiling from a high energetic photon [20]. These events are selected in 41.1 fb^{-1} of proton-proton collisions at a center-of-mass energy of $\sqrt{s} = 13 \text{ TeV}$ using a single photon trigger with p_{T} threshold of 175 GeV which translates to a 200 GeV p_{T} requirement for the offline reconstructed photon to be at plateau of the trigger efficiency. Thanks to the cleaner photon signature, the leading AK8 jet p_{T} requirement, equivalent to the photon p_{T} , is lower than the one used in hadronic ISR-based analyses, as a consequence upper limits are placed on the quark coupling for masses as low as 10 GeV.

ATLAS as well performed a search for low mass resonances produced in association with either a photon or a high energetic ISR jet, using an integrated luminosity of 36.1 fb^{-1} at a center-of-mass energy of $\sqrt{s} = 13 \text{ TeV}$ [21]. The trigger requires either an isolated photon with transverse energy $E_{\text{T}} > 140 \text{ GeV}$ or an anti- k_{T} jet with radius parameter $R = 0.4$ (AK4) and $p_{\text{T}} > 280 \text{ GeV}$. The resonance is searched as an excess in the distribution of the large-radius jet masses, reconstructed with the anti- k_{T} algorithm of radius $R=1.0$ (AK1.0) and requiring $p_{\text{T}} > 200 \text{ GeV}$, in the mass range between 100 GeV and 220 GeV. ATLAS searched for resonance decaying into $b\bar{b}$ pairs using 79.8 fb^{-1} of data recorded at a center-of-mass energy of $\sqrt{s} = 13 \text{ TeV}$ with a single photon trigger and 76.6 fb^{-1} with a photon plus jet trigger [22]. The resonance is considered to recoil from the photon and to decay into two distinct reconstructed AK4 jets with transverse momentum $p_{\text{T}} > 25 \text{ GeV}$ jets which contain b -hadrons (b -jets) are identified using specialised algorithms (b -tagged). Given the sizable angular separation between individual jets the mass range probed for the presence of a Z' axial-vector dark-matter mediator range from 169 to 1100 GeV. Note that

the expected sensitivity for the b -tagged analysis is better than the flavour-inclusive, non b -tagged analysis, even for Z' models where the Z' equally decay into all quark flavours.

CMS also searched for a low mass resonance decaying into $b\bar{b}$ pairs recoiling from an ISR jet in events recorded at a center-of-mass energy of $\sqrt{s} = 13$ TeV corresponding to a luminosity of 35.9 fb^{-1} of data [23] using a combination of several triggers whose full efficiency condition requires the p_T of the large-radius jet used for reconstructing the resonance mass to be larger than 450 GeV. A dedicated double- b -tagger is used to select jets likely to originate from two b -quarks. No significant excess above the SM prediction is observed for signal masses between 50–350 GeV and limits were set in this region.

In this work, we present a sensitivity study for the search of pseudoscalar resonances decaying to $b\bar{b}$ pairs in proton-proton collisions at a center-of-mass energy of $\sqrt{s} = 14$ TeV and an integrated luminosity of 3000 fb^{-1} , achievable at the end of the High Luminosity LHC (HL-LHC) data taking, using a parametrised ATLAS detector simulation. We perform our analysis focusing on the sensitivity for $b\bar{b}$ resonances with mass values ranging from 10 GeV to 100 GeV. In this mass range, we adopt a strategy based on triggering on a high- p_T photon and we look for a recoiling large-radius jet that contains collimated $b\bar{b}$ pairs. As discussed before, this is an optimal strategy, given the lower achievable photon threshold at trigger level with respect to choosing ISR jets, it can probe efficiently masses $\gtrsim 10$ GeV. Moreover, the $b\bar{b}$ final state is the dominant decay channel for spin-0 particles with Yukawa-like couplings to fermions and masses below the top-quark mass. To be noticed that the analysis proposed is an extension of the current landscape of light $b\bar{b}$ resonance searches.

The structure of the paper is organised as follows. Section 2 presents the model of interest, which features a light pseudoscalar with Yukawa-like coupling structure to fermions. In Section 3, we present a collider analysis for the pseudoscalar decaying to $b\bar{b}$ final state. Section 3.1 details the simulation of signal and background events. The event selection criteria is presented in Section 3.2 together with the description of jet substructure observables used to reject background events. In Section 3.3, the emulation of b -tagging algorithms are presented on simulated events, together with the labelling scheme used to categorise the AK1.0 jets according to the *flavour*. A fit is performed on the signal mass distribution in Section 3.4, and the signal efficiencies and background yields are estimated after the analysis requirements. Section 4 presents the sensitivity of the analysis to exclude a $b\bar{b}$ resonance at the HL-LHC, including a modified trigger requirement to further enhance the sensitivity in Section 4.2. The importance of the results are interpreted with respect to the existing bounds in Section 4.3. Finally, we summarise our findings in Section 5, draw conclusions and outline future directions.

2 Light pseudoscalar: model and motivations

The model we study consists of a light pseudoscalar, also referred as axion-like particle (ALP). We consider this particle a to couple only to SM fermions, and assume these couplings to be proportional to the fermion mass,

$$\mathcal{L}_{\text{ALP}} \supset \frac{1}{2} \partial_\mu a \partial^\mu a - \frac{1}{2} m_a^2 a^2 + i \sum_f g_{\text{aff}} m_f a \bar{f} \gamma_5 f, \quad (2.1)$$

where m_a is the mass of the ALP, and g_{aff} is a real, dimensionful parameter, $g_{\text{aff}} = \frac{C_f}{f_a}$, with C_f dimensionless and f_a an energy scale, typically the spontaneous-symmetry-breaking scale associated with the ALP. Assuming $C_f \lesssim \mathcal{O}(1)$ and f_a is greater than the EW symmetry breaking scale, one obtains an approximate theoretical upper limit of $g_{\text{aff}} \lesssim 0.01 \text{ GeV}^{-1}$.

We assume C_f to be universal for all SM fermions. This assumption is motivated by the following argument [3, 24–26]. If the ALP interactions respect a shift symmetry, $a \rightarrow a + c$ (as expected for Nambu-Goldstone bosons), and if one requires a principle of minimal flavour violation (to circumvent experimental constraints on flavour and CP violation), then the ALP couplings to SM quarks have to be proportional to the quark Yukawa couplings,

$$\mathcal{L}_{\text{ALP}} \supset i \frac{a}{f_a} \left(C_d \bar{q}_L Y_d d_R H + C_u \bar{q}_L Y_u u_R \tilde{H} + h.c. \right), \quad (2.2)$$

with $C_{d,u}$ real constants, up to corrections involving higher powers of $Y_{d,u}$. Now, replacing the Higgs doublet H by its vacuum expectation value, and diagonalising the quark mass matrices, one is led to Eq. (2.1), with $C_d = C_s = C_b$ and $C_u = C_c = C_t$. In our analysis we will take for simplicity $C_d = C_u$ but, as we are interested in ALP decays to b quarks, one could suppress C_u , to avoid potential, indirect constraints on ALP couplings to the up quark, as obtained in Ref. [27] (see discussion in Section 4.3). The Yukawa-like couplings of the ALPs to fermions imply that for ALPs with masses between twice the bottom mass and twice the top mass, $2m_b < m_a < 2m_t$, the dominant decay is $a \rightarrow b\bar{b}$. This motivates LHC searches for $\mathcal{O}(10 - 100) \text{ GeV}$ resonances decaying to $b\bar{b}$ final states. In order to trigger on this final state, we require an initial state photon, as further discussed in Section 3.

Note that such an ALP could also couple to DM, as studied for the case of fermionic DM in e.g. Refs. [10, 28]. The Lagrangian takes the form

$$\mathcal{L} = \mathcal{L}_{\text{SM}} + \mathcal{L}_{\text{ALP}} + \bar{\chi}(i\not{\partial} - m_\chi)\chi + i \frac{C_\chi}{f_a} m_\chi a \bar{\chi} \gamma_5 \chi, \quad (2.3)$$

where the DM particle χ of mass m_χ couples to the ALP via the coupling C_χ . Depending on the couplings of the ALP to DM and to the SM, the production mechanism changes. In freeze-out, one has large enough ALP couplings such that equilibrium is obtained between the hidden sector particles and SM, whereas in freeze-in, the couplings are small, such that DM-SM equilibrium is never achieved. In both cases, the relic density may depend on the ALP to DM thermal cross-section or the SM to DM thermal cross-section, depending on

which of these are dominant. Considering the $m_a - g_{\text{aff}}$ plane, it was found in Ref. [10] that a large range of parameter space, where the correct relic density via freeze-in can be obtained, remains allowed, particularly for values of m_a above $\mathcal{O}(10)$ GeV. Note that for the values of g_{aff} close to the theoretical upper limit of $g_{\text{aff}} \lesssim 0.01 \text{ GeV}^{-1}$ (which could be probed at colliders) dark matter production via fermion scattering is relevant. It was seen in Ref. [10] that in this region there is a large hierarchy between g_{aff} and $g_{a\chi\chi}$, which would need to be explained via further model building.

The sensitivity study performed in this work is presented in terms of the above-discussed ALP model. However, pseudoscalars with masses below the electroweak scale and couplings to fermions are also motivated by theories addressing the stability of the electroweak scale, such as Higgs compositeness. In fact, a composite Higgs boson requires the introduction of a new strongly-coupled sector close to the TeV scale, whose spectrum contains several composite resonances, including SM singlets that may be lighter than the Higgs itself. In this context, a particularly well-motivated target for low mass resonance searches is a pseudo Nambu-Goldstone boson a , analogous to a QCD pion, whose small mass arises radiatively, via shift-symmetry breaking couplings. Indeed, the couplings of the a to b -quarks induce $m_a \gtrsim 10 \text{ GeV}$ [12, 13] at one loop, as desired. Note that here we are referring to additional ALP couplings, which break the Nambu-Goldstone shift symmetry, thus inducing a non-trivial potential. Such a composite pseudoscalar has been searched for at colliders, but mostly using large- p_T signatures which require m_a above the electroweak scale [14]. An interesting study to probe m_a well below the electroweak scale at LHCb can be found in Ref. [15], which exploits decay channels other than $b\bar{b}$.

3 Collider Analysis

This work focuses on the search of a light pseudoscalar, in the mass range between 10 GeV and 100 GeV, decaying to $b\bar{b}$ pairs as predicted in the ALP model described in Section 2, at the LHC. In order to reconstruct its decay products, the low mass resonance is required to be in a boosted regime, where the produced b -hadrons from the ALP are collimated. Kinematically this can be achieved by demanding that the ALP is produced together with a high energetic recoiling object, either a photon or an ISR jet. The signal in the current analysis encompasses a high p_T isolated photon produced back-to-back to a large radius jet having two prong jet substructure from hadronisation objects of two b -quarks. The Feynman diagram of the hard process for signal production, $pp \rightarrow a(\rightarrow b\bar{b})\gamma$, is shown in Fig. 1 (a)¹.

The dominant background arises from multijet production in association with a photon. In Fig. 1 (b), we show one of the Feynman diagrams for the γ +multijet process. Subdominant resonant backgrounds originate from $W + \gamma$ and $Z + \gamma$ processes (see Fig. 1

¹We showed only the $q\bar{q}$ initial state, because the putative gluon fusion diagram for γ +ALP production vanishes. Indeed, the ALP couplings to quarks, C_q , allow for gluon-gluon fusion to produce an ALP via a triangle loop of quarks, an effect dominated by the top quark loop. However, we are interested in the ALP production associated with a photon, which rather involves a box loop of quarks, and the latter vanishes as a consequence of the generalised Furry's theorem [29].

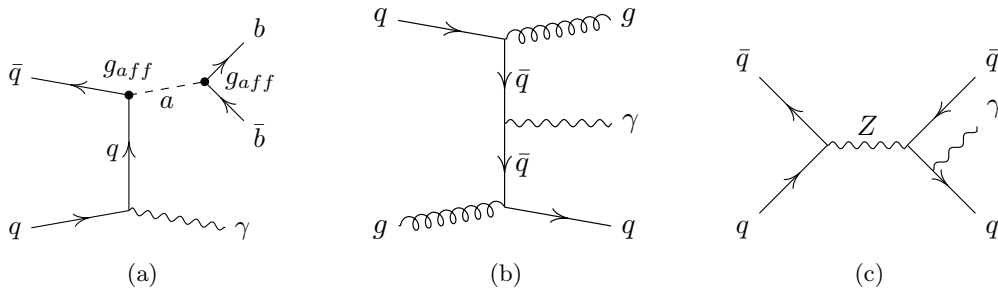


Figure 1: (a) The Feynman diagram for the signal process, $pp \rightarrow a(\rightarrow b\bar{b})\gamma$, where the ALP-fermion couplings, g_{aff} , are shown, and one representative Feynman diagram for the (b) non-resonant and (c) resonant background, $pp \rightarrow jj\gamma$.

(c)). In the following subsections, we discuss the generation of signal and background processes, the physics object used in the analysis, kinematic observables, the event selection criteria and finally the details of the b -tagging simulation. The section ends with the estimation of the signal and background yields.

3.1 Event simulation

Signal and SM background processes are simulated using Monte Carlo (MC) event generators. The γ +ALP signal process $pp \rightarrow a(\rightarrow b\bar{b})\gamma$ is generated using `MadGraph5_aMC@NLO` [30] at leading order (LO). The γ +multijet background process, which include both non-resonant and resonant $W/Z + \gamma$ processes, is simulated using `Pythia8` [31]. Both signal and background are generated in the 5F scheme where proton contains gluon, light- and b -quarks. The center-of-mass energy considered for the proton-proton collisions is $\sqrt{s} = 14$ TeV. To simulate the showering and hadronisation effects, the generated events are interfaced with `Pythia8`, with the `A14` tune [32], and the parton distribution function (PDF) set `NNPDF2.3NLO` [33] is used. Finally, the detector simulation is performed with `Delphes-3.5.0` [34] using the default HL-LHC ATLAS analysis card. We apply specific requirements for the generation of the signal and background events to improve the statistics in the phase space relevant to the proposed analysis. The inclusive cross-sections and generation-level cut efficiencies for the $pp \rightarrow a(\rightarrow b\bar{b})\gamma$ signal process is shown in Table 1.

In order to produce on-shell light pseudoscalar, decaying into two b -hadrons, we restrict the lowest ALP mass to $m_a > 2m_{B^0/B^\pm} \simeq 10.6$ GeV. Specifically, we choose the following benchmark masses for the ALP, $m_a = 12$ GeV and then from 20 GeV to 100 GeV in steps of 10 GeV. The ALP-fermion coupling, g_{aff} is fixed to 0.1 GeV^{-1} and the total decay width of the ALP for each benchmark mass is taken from Ref. [10].

3.2 Object definitions and event selection

At selection level, a large radius jet for full containment of the hadronisation products, coming from the final state b -quarks, is required. The reconstruction of jets is performed within the `FastJet` framework [35], utilizing the `AK1.0` anti- k_T clustering algorithm, using

$pp \rightarrow a(\rightarrow b\bar{b})\gamma$		
m_a [GeV]	σ ($g_{\text{aff}} = 0.1 \text{ GeV}^{-1}$) [pb]	ϵ ($\times 10^{-5}$)
12	15264 ± 113	0.07
20	9727 ± 82	0.13
30	4690 ± 43	0.27
40	2454 ± 22	0.48
50	1343 ± 13	0.79
60	779 ± 7	1.22
70	472 ± 5	1.78
80	294 ± 3	2.49
90	191 ± 2	3.34
100	128 ± 1	4.35

Table 1: The inclusive cross-section (σ) for $pp \rightarrow a(\rightarrow b\bar{b})\gamma$ production, and generation cut efficiency (ϵ) which is defined as the ratio of cross-section after the generation cuts to the inclusive one. The errors associated with inclusive cross-sections are obtained from **MadGraph5**. The generation cuts are as follows: $p_{T,j} > 5 \text{ GeV}$, $p_{T,\gamma} > 160 \text{ GeV}$, $|\eta_{j/\gamma}| < 3.0$, $\Delta R_{jj} > 0.01$, $\Delta R_{j\gamma} > 1.0$. Here, p and j both contain gluon, light quarks and b -quark.

the particle-flow objects in Delphes as input. The photon, used to trigger on, is required to have $p_{T,\gamma} > 160 \text{ GeV}$ and $|\eta_\gamma| < 2.1$ [20, 21]. Further, a separation between the photon and AK1.0 jet is required to be $\Delta R > 2.2$ ² [20]. We apply the soft drop mass algorithm [36] to groom the AK1.0 jet, using the parameters $z_{\text{cut}} = 0.1$ and $\beta = 1$ [37] where, z_{cut} denotes the energy threshold required to satisfy the soft drop condition during the declustering procedure. The soft drop condition is defined as $\frac{\min(p_{T,1}, p_{T,2})}{p_{T,1} + p_{T,2}} > z_{\text{cut}} \left(\frac{\Delta R_{12}}{R_0}\right)^\beta$. Here, $p_{T,i}$ are jet constituents' transverse momentum, ΔR_{12} is the angular separation between those constituents and R_0 is the jet radius parameter. The angular exponent $\beta \neq 0$ imposes an additional angular requirement on the soft drop condition. Specifically, the soft drop removes soft wide angle radiation from a jet, while keeping a fraction of the soft collinear radiation as long as $\beta > 0$. Although the $\beta = 0$ choice is widely used [20], this choice significantly reduces the signal efficiency for lowest ALP mass ($m_a = 12 \text{ GeV}$) considered in this analysis while $\beta = 1$ is found to be optimal across the entire mass range. Fig. 2 represents the distribution of m_{SD} , the invariant mass of the soft dropped AK1.0 jet. As shown, by removing the soft radiation, the grooming technique softens the m_{SD} spectrum of multijet events, while it leaves the signal distribution almost unaltered.

In case of signal events, the two b -quarks from the ALP decay originate a clear 2-prong

²The angular distance in the pseudorapidity (η) and azimuthal angle (ϕ) plane is measured in units of $\Delta R = \sqrt{(\Delta\eta)^2 + (\Delta\phi)^2}$. Here, η is defined in terms of polar angle (θ) as $\eta = -\ln \tan(\theta/2)$.

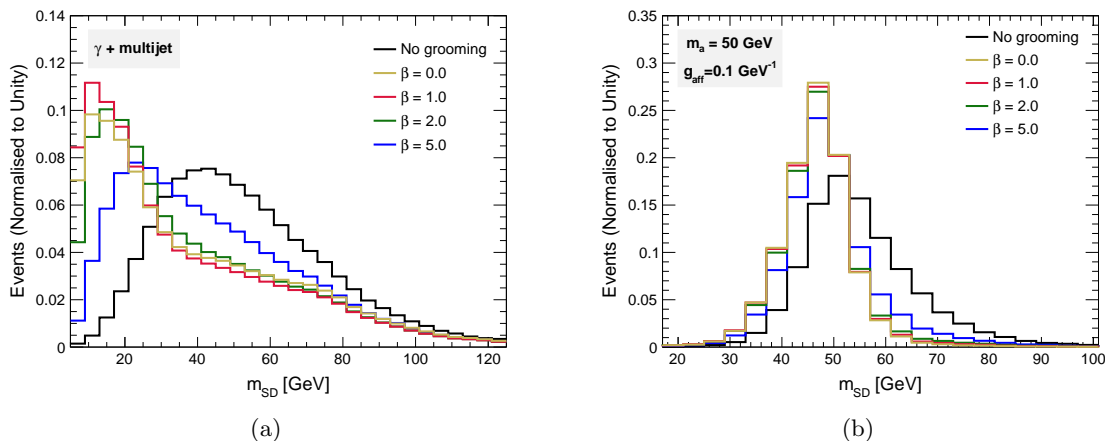


Figure 2: The soft drop mass distributions of AK1.0 jet by changing the soft drop parameter β , with fixed $z_{cut} = 0.1$, (a) for the multijet background, and (b) ALP signal of mass $m_a = 50$ GeV.

substructure signature that can be reconstructed within the AK1.0 jet. However, that is not the case for multijet background, where the final state features collimated radiation with merged hadronisation objects. The designed decorrelated tagger (DDT) [38, 39] observable N_2^{DDT} , defined as

$$N_2^{\text{DDT}}(\rho, p_T) \equiv N_2 - N_2^{10\%}(\rho, p_T), \quad (3.1)$$

is used in the following, where N_2 is a 2-prong discriminating observable and $N_2^{10\%}$ is the value of N_2 that rejects 90% of the multijet background events, which depends on the jet p_T and the scaling variable ρ . The observable, N_2 is constructed as the ratio of generalised energy correlation functions (ECF) [40] as

$$N_2 = \frac{{}_2e_3}{{}_1e_2^2}, \quad (3.2)$$

where the two point and three point ECFs, ${}_1e_2$ and ${}_2e_3$ are defined as

$$\begin{aligned} {}_1e_2 &= \sum_{1 \leq i < j \leq N} z_i z_j \Delta R_{ij}, \\ {}_2e_3 &= \sum_{1 \leq i < j < k \leq N} z_i z_j z_k \min \{ \Delta R_{ij} \Delta R_{ik}, \Delta R_{ij} \Delta R_{jk}, \Delta R_{ik} \Delta R_{jk} \}. \end{aligned} \quad (3.3)$$

Here, z_i is the energy fraction of i th jet constituent, $z_i \equiv \frac{p_{T,i}}{p_{T,\text{jet}}}$ and ΔR_{ij} corresponds to the separation between the i th and j th jet constituents in the $\eta - \phi$ plane. In general, ${}_2e_3$ depends on the n energy fractions of the N constituent particles inside the jet ($n \leq N$), relative to the jet p_T and the minimal product of v number of pairwise angles between the n selected particles. In a scenario where there is a perfect two-prong structure inside the jet, $({}_1e_2)^2 \gg {}_2e_3$ [40], therefore the smaller value of N_2 in signal events can be

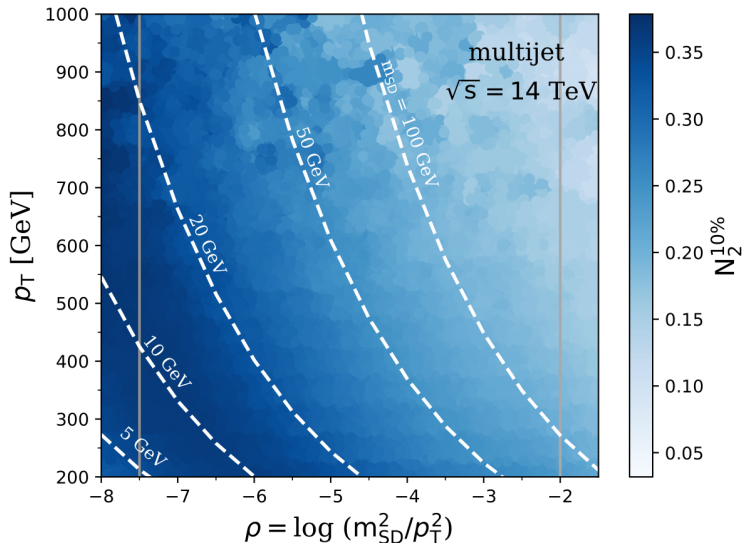


Figure 3: The 10% quantile of the N_2 distribution in simulated multijet events, $N_2^{10\%}$, used to define the N_2^{DDT} variable. The distribution is shown in the $\rho - p_T$ plane. The white dashed lines correspond to constant values of the jet mass, m_{SD} . We select the region $-7.5 < \rho < -2.0$ for our analysis, as shown with vertical gray lines.

used as discriminant against multijet background. At analysis level, in order to reduce the variable’s dependency on the jet mass and transverse momentum, the N_2 variable is estimated on the groomed AK1.0 jet.

The dimensionless scaling variable ρ defined as $\rho = \log(m_{\text{SD}}^2/p_T^2)$ [38] is designed to reject events having non-perturbative effects in the QCD jet mass spectrum. The selected ρ region in the analysis is $-7.5 \leq \rho \leq -2.0$, which is efficient for the signal process, and it corresponds to our region of interest, with m_{SD} from 5 GeV to 100 GeV, for AK1.0 jet with $p_T = 200$ GeV. $N_2^{10\%}$, shown in Fig. 3, is evaluated in multiple bins of the $\rho - p_T$ plane. Smoothing, using the distance-weighted k -nearest-neighbor (kNN) rule [41], is applied to $N_2^{10\%}$, to efficiently populate all the phase space. The signal efficiency of the $N_2^{\text{DDT}} < 0$ requirement, varies roughly between 12% and 26%, increasing the signal over background ratio, since by construction only 10% of the background are retained, with the exception of $m_a = 12$ GeV for which the efficiency drops to $\sim 1\%$. For the latter, given the high p_T of the AK1.0 jet, the b -quarks from the ALP decay are so collimated that the two-prong structure is lost, resulting in a large loss in efficiency after the N_2^{DDT} requirement. We will show later that this can be partly recovered if a lower threshold for the trigger photon can be achieved by the LHC experiments.

After the requirements listed in Table 2, we show the mass distribution, m_{SD} , for the multijet background and ALP signal, normalized to $\mathcal{L} = 3000 \text{ fb}^{-1}$ of proton-proton collisions at center-of-mass energy \sqrt{s} of 14 TeV, in Fig. 4. The shape of the m_{SD} distribution for multijet events was found in good agreement with Ref. [20, 39], correspondingly, we

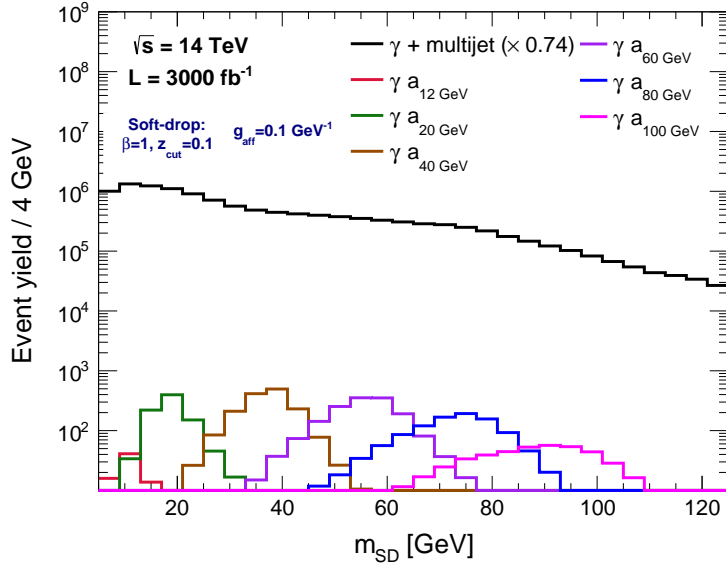


Figure 4: The soft drop mass distributions of AK1.0 jet for the multijet background and ALP signal. The ALP signals are shown as γa_{m_a} , for example, $\gamma a_{12 \text{ GeV}}$ corresponds to signal process with $m_a = 12 \text{ GeV}$. The γ +multijet background includes contributions from $W + \gamma$ and $Z + \gamma$ processes. The event yield on the y-axis is evaluated after all the selection cuts (see Table 2). The background distribution is corrected with an overall factor of 0.74 [39].

apply a data-Monte Carlo scale factor of 0.74 [39] to the multijet background cross-section as estimated by Pythia8, which after the generation requirements is 323 pb. The mass distributions of the ALP signal are shown for $g_{\text{aff}} = 0.1 \text{ GeV}^{-1}$, for some benchmark masses of ALP. It can be noticed that as the generated ALP mass increases, the variance of the m_{SD} resonance distribution increases as well. This can be understood as the cone size of the AK1.0 jet, with radius parameter $R = 1.0$, starts to be insufficient to encompass all the hadronisation objects from a heavy ALP decay recoiling from a photon with $p_T > 160 \text{ GeV}$, as the ALP becomes less boosted.

3.3 Flavour labelling and b -tagging on the simulated events

Identifying hadronic jets containing b -hadrons (b -tagging), is an essential tool to improve signal sensitivity in searches where the final state contains b -quarks. The ATLAS and CMS experiments utilise highly performing Neural Network-based b -tagging algorithms [42, 43] in many Higgs, Supersymmetry, top-quark analyses [44–49]. The search for boosted Higgs production [50] at the LHC using GN2X double b - and double c -tagging algorithms is taken as a reference for the ALP analysis proposed in this work.

Delphes, used for simulating the detector reconstruction, not having tracking reconstruction capability, uses a flavour dependent parametrized single jet b -tagging probability based on ATLAS and CMS published performance [51, 52]. The emulation of double b -tagging is developed and applied outside Delphes by the authors of this work. In par-

Selection requirements	
$p_{T,\gamma}$	$> 160 \text{ GeV}$
$ \eta_\gamma $	< 2.1
$p_{T,\text{AK1.0}}$	$> 200 \text{ GeV}$
$\Delta R(\gamma, \text{AK1.0})$	> 2.2
ρ	$[-7.5, -2.0]$
N_2^{DDT}	< 0

Table 2: Summary of the selection requirements. The transverse momentum of the photon and AK1.0 jet is denoted as $p_{T,\gamma}$ and $p_{T,\text{AK1.0}}$, respectively, and distance between them is referred as $\Delta R(\gamma, \text{AK1.0})$. η_γ is the pseudorapidity of the photon. ρ is a dimensionless scaling variable, $\rho = \log(m_{\text{SD}}^2/p_T^2)$. The DDT observable is represented as N_2^{DDT} .

ticular, we use a parametrisation of the boosted double b - and double c -tagging algorithm with a working point of 80% bb tagging efficiency. The corresponding rejection efficiencies for multijet background are taken from the GN2X performance listed in Ref. [50]. The parametrisation involves identifying smaller radius jets, called subjets, inside the AK1.0 jet and matching them to a hadron in the event to identify different double flavour jet categories, and it is explained in what follows.

The multijet background events which passes the soft-drop grooming and $N_2^{\text{DDT}} < 0$ requirements, discussed Section 3.2, mostly contain AK1.0 jets presenting a two prong substructure. These may originate from the initial state partons in the following three ways: two quarks (qq' , $q/q' = u, d, c, s, b$), or a quark and a gluon (qg), or two gluons (gg), produced back-to-back to the high p_T photon. In order to categorise the flavour content of these events, ATLAS uses variable radius (VR) anti- k_T jets [53, 54], since fixed radius jet algorithms [19, 55, 56] introduce overlapping subjets and reduce the efficiency for flavour labelling in case of low ALP mass where the decay products are highly collimated.

The VR algorithm can differentiate the substructure coming from a hard parton than from soft radiation because the radius of the constructed jet changes according to the jet transverse momentum. Three parameters are required to define the VR subjets: ρ_{VR} , R_{min} and R_{max} . ρ_{VR} is a dimensionful constant and the effective jet radius depends on the jet transverse momentum as, $R_{\text{eff}}(p_T) = \rho_{\text{VR}}/p_T$. The parameters, R_{min} and R_{max} , ensure that the effective jet radius do not fall below the detector resolution at high p_T and jets do not become arbitrarily large at small p_T , respectively. These three parameters need to be optimised to improve signal acceptance or background rejection for specific scenarios. The minimum and maximum values for the radius parameter are optimised in Ref. [54] and we use them in our analysis, $R_{\text{min}} = 0.02$ and $R_{\text{max}} = 0.4$. However, we optimise ρ_{VR} in the following paragraph since a wide range of masses for the ALP signal are considered in this work.

We choose ρ_{VR} to maximise the double subjet b -labelling efficiency, as a function of the

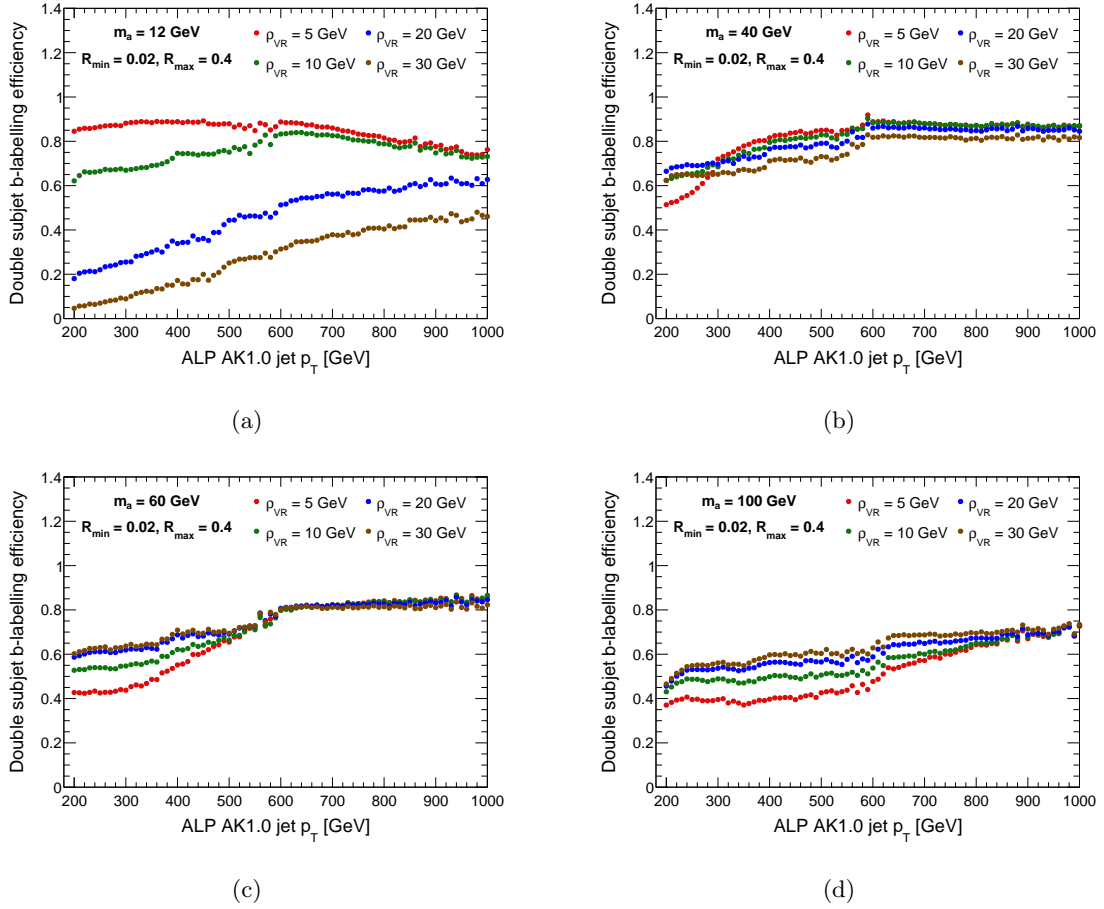


Figure 5: Comparison of double subject b -labelling efficiency for different choices of the ρ_{VR} parameter while constructing the VR subjects. The efficiencies are shown for the simulated ALP signal with masses, (a) $m_a = 12$ GeV, (b) $m_a = 40$ GeV (c) $m_a = 60$ GeV and (d) $m_a = 100$ GeV. The R_{\min} and R_{\max} values are set to 0.02 and 0.4 [54], respectively.

transverse momentum of the AK1.0 jet. The efficiency is defined as the ratio between the number of AK1.0 jets having two b -subjects with $p_{T,\text{subject}} > 7$ GeV and the total number of AK1.0 jets. The flavour matching procedure is discussed in the following paragraph ³. A comparison of these efficiencies for different choices of the ρ_{VR} parameter is shown in Fig. 5 for ALP masses of 12 GeV, 40 GeV, 60 GeV and 100 GeV. A smaller ρ_{VR} value is preferred for a light ALP, while the efficiency is higher with larger ρ_{VR} parameter for a heavier ALP. These preferred choices for the ρ_{VR} value, specifically $\rho_{VR} = 5$ GeV for $m_a = 12$ GeV, 20 GeV and 30 GeV; $\rho_{VR} = 10$ GeV for $m_a = 40$ GeV and 50 GeV; $\rho_{VR} = 20$ GeV for $m_a = 60$ GeV and 70 GeV; $\rho_{VR} = 30$ GeV for $m_a = 80$ GeV, 90 GeV and 100 GeV; are used while constructing the two subjects with the VR algorithm, for both the signal and

³Note that the same flavour matching method is used first to set the optimal ρ_{VR} parameter, and later to categorise the AK1.0 jet into different flavour composition.

VR parameters	
$p_{T,\text{subjct}}$	$> 7 \text{ GeV}$
R_{min}	0.02
R_{max}	0.4
$m_a \text{ [GeV]}$	$\rho_{\text{VR}} \text{ [GeV]}$
12, 20, 30	5
40, 50	10
60, 70	20
80, 90, 100	30
Matching parameters	
$p_{T,\text{hadron}}$	$> 5 \text{ GeV}$
$\Delta R(\text{hadron, VR})$	< 0.3
$\Delta R(\text{hadron/VR, AK1.0})$	< 1.0

Table 3: Summary of the parameters used in variable radius (VR) subjet construction (top panel) and the matching procedure (bottom panel). The radius parameter for the VR subjet is $R_{\text{eff}}(p_T) = \rho_{\text{VR}}/p_T$. The transverse momentum of the VR subjet is $p_{T,\text{subjct}}$. The minimum and maximum radius parameters in the VR algorithm are R_{min} and R_{max} , respectively. If a b -hadron is found, the jet is called b -jet, otherwise if a c -hadron is found, the jet is called c -jet, if no c - or b -hadrons are present the jet is referred to as light jet. Here, jet refers to the VR subjets.

multijet background.

Next, we match each VR subjet to a hadron. We first identify b -hadrons and c -hadrons in the event which originate from quark hadronisation, with $p_{T,\text{hadron}} > 5 \text{ GeV}$ and within $\Delta R < 1.0$ of the AK1.0 jet axis. Events are selected if they contain at least two VR subjets with $p_{T,\text{subjct}} > 7 \text{ GeV}$, similar to earlier double subjet b -labelling efficiency, and the subjets fall inside the AK1.0 jet. Thus the selected events have at least two VR subjets and identified hadrons within $\Delta R < 1.0$ of the AK1.0 jet. The VR subjet is called b -jet (**b**) when a b -hadron is found within $\Delta R < 0.3$ [57] of the VR subjet. If there is no nearby b -hadron but a c -hadron is found with $\Delta R(c\text{-hadron, VR-subject}) < 0.3$, the VR subjet is labelled as c -jet (**c**). In case the b -hadron or c -hadron is within $\Delta R < 0.3$ of multiple VR subjets, the hadron is associated to the closest VR subjet. Otherwise, the VR subjet is labelled as a light jet (**l**). We summarise all the above discussion in Table 3.

Since we have at least two flavour matched VR subjets, the AK1.0 jets can be broken down to the following flavour compositions: bb , bc , bl , cc , cl , and ll . The signal events having at least two VR subjets inside the AK1.0 jet labelled as b -jets (bb) are approximately 71% for a 12 GeV ALP signal, which increases to around 90% for $m_a = 20 \text{ GeV}$ and 30

Multijet background						
Category	bb	bc	bl	ll	cl	cc
Fractional composition (%)	0.6	0.5	1.2	84.4	10.5	2.8
GN2X efficiency [50]	0.59	0.21	0.07	0.21×10^{-3}	0.41×10^{-2}	0.02

Table 4: The fraction of AK1.0 jets in the multijet sample, sorted by flavour composition, that have at least two VR subjets. The values are shown for $\rho_{\text{VR}} = 30$ GeV and remain roughly the same with different choices of the ρ_{VR} parameter. The GN2X efficiency for background in each category are shown for the working point of 80% bb tagging efficiency, from Ref. [50].

GeV. The percentage of signal events passing that criteria decreases gradually afterwards, reducing down to roughly 62% for $m_a = 100$ GeV, since the jet radius becomes insufficient to include all hadronisation objects, particularly for heavier ALP (see Fig. 5). In the case of the multijet sample, around 85% of the AK1.0 jets have no b - or c -subjets. The fraction of AK1.0 jets with subjet flavour in the various categories is tabulated in Table 4, for $\rho_{\text{VR}} = 30$ GeV. The fractional values hardly change with ρ_{VR} parameter.

3.4 Signal extraction and background estimation

The final search is performed by selecting a mass window around the ALP reconstructed m_{SD} mass variable after all selection requirements listed in Table 2. For each mass point, we estimate the m_{SD} resolution using a double-sided Crystal Ball function [58, 59], which is found to be robust against the change in shape of the resonance peak for different ALP masses. The Crystal Ball function, consists of a Gaussian function to fit the core of the distribution in combination of a power law function to fit both the low and high m_{SD} regions. The Crystal Ball function is defined as:

$$f(m_{\text{SD}}|N, \mu, \sigma, \alpha_{\text{low}}, \alpha_{\text{high}}, n_{\text{low}}, n_{\text{high}}) =$$

$$N \times \begin{cases} e^{-0.5\left(\frac{m_{\text{SD}}-\mu}{\sigma}\right)^2}, & \text{if } -\alpha_{\text{low}} \leq \frac{m_{\text{SD}}-\mu}{\sigma} \leq \alpha_{\text{high}}, \\ e^{-0.5\alpha_{\text{low}}^2 \left[\frac{\alpha_{\text{low}}}{n_{\text{low}}} \left(\frac{n_{\text{low}}}{\alpha_{\text{low}}} - \alpha_{\text{low}} - \frac{m_{\text{SD}}-\mu}{\sigma}\right)\right]^{-n_{\text{low}}}}, & \text{if } \frac{m_{\text{SD}}-\mu}{\sigma} < -\alpha_{\text{low}}, \\ e^{-0.5\alpha_{\text{high}}^2 \left[\frac{\alpha_{\text{high}}}{n_{\text{high}}} \left(\frac{n_{\text{high}}}{\alpha_{\text{high}}} - \alpha_{\text{high}} + \frac{m_{\text{SD}}-\mu}{\sigma}\right)\right]^{-n_{\text{high}}}}, & \text{if } \frac{m_{\text{SD}}-\mu}{\sigma} > \alpha_{\text{high}}, \end{cases} \quad (3.4)$$

where N is an overall normalisation parameter. The Gaussian part of the Crystal Ball distribution has mean value μ and width σ , while α_{low} and α_{high} parameterise the points where the power law function takes over. The corresponding exponents of the power law function are denoted as n_{low} and n_{high} , respectively. In Fig. 6, we show the m_{SD} distribution for the simulated signal samples, together with their corresponding Crystal Ball fit, for ALP masses of 20 GeV, 40 GeV, 60 GeV, 80 GeV and 100 GeV.

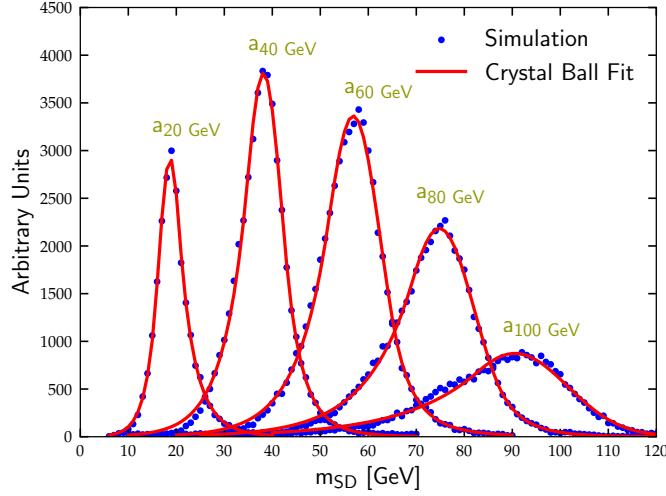


Figure 6: The m_{SD} distribution for the simulated signal samples and the Crystal Ball fits, in blue and red color, respectively. The fits are shown for signal events with $m_a = 20, 40, 60, 80$ and 100 GeV, after all the requirements mentioned in Table 2.

m_a [GeV]	Fitted parameters [GeV]		ϵ ($\times 10^{-2}$)	Yield at $\mathcal{L} = 3000 \text{ fb}^{-1}$	
	μ	σ		S ($g_{\text{aff}} = 0.1 \text{ GeV}^{-1}$)	N_B
12	10.91 ± 0.16	2.21 ± 0.17	0.10	30	4040
20	18.70 ± 0.03	2.46 ± 0.05	1.00	400	7820
30	28.22 ± 0.03	3.39 ± 0.04	1.50	590	7550
40	38.16 ± 0.04	3.95 ± 0.07	1.90	660	7810
50	47.68 ± 0.03	4.68 ± 0.05	2.20	710	11000
60	56.86 ± 0.06	5.76 ± 0.08	2.40	670	11310
70	66.19 ± 0.06	6.70 ± 0.08	2.20	550	11620
80	74.80 ± 0.07	7.33 ± 0.10	1.80	400	11770
90	82.01 ± 0.13	9.62 ± 0.14	1.60	310	11970
100	90.55 ± 0.20	10.96 ± 0.21	1.10	180	7310

Table 5: The mean values, μ and widths, σ obtained after fitting the ALP reconstructed m_{SD} mass variable with the Crystal Ball function, along with the signal efficiency, ϵ . The signal yields, S for $g_{\text{aff}} = 0.1 \text{ GeV}^{-1}$ and background yields, N_B , are also shown at integrated luminosity of 3000 fb^{-1} , for the simulated MC samples.

The mass window, defined as the interval $[\mu - \sigma, \mu + \sigma]$, is used for the search of each ALP mass hypothesis and is tabulated in Table 5, together with the corresponding signal efficiency and multijet background yield for proton-proton collisions at center-of-mass energy $\sqrt{s} = 14$ TeV and 3000 fb^{-1} of integrated luminosity. As discussed earlier, the low signal efficiency at $m_a = 12$ GeV results from the lack of 2-prong substructure at high jet p_T and therefore a low N_2^{DDT} efficiency. To be noticed that since for high values of the ALP mass, the decay products tend to be less collimated, and therefore less likely to be contained in the cone of the AK1.0 jet, the width of the m_{SD} distribution increases.

4 Results

In this section, we present our final results in terms of 95% confidence level (CL) upper exclusion limits on the $b\bar{b}\gamma$ production cross-section and the ALP-fermion coupling, g_{aff} . The exclusion limits are evaluated in Section 4.1. We further discuss how to improve the sensitivity by lowering the photon p_T threshold in Section 4.2. The results are complemented with astrophysical and collider bounds in Section 4.3.

4.1 Projected sensitivities on the cross-section and coupling

The upper limit on the cross-section is evaluated with the signal significance formula [60, 61], $S/\sqrt{N_B} > N_{\text{CL}}$, where $N_{\text{CL}} = 2$ corresponds to 95% confidence interval. The signal yield, S can be computed as:

$$S = \sigma(pp \rightarrow a\gamma \rightarrow b\bar{b}\gamma) \cdot \epsilon \cdot \mathcal{L} ,$$

where $\sigma(pp \rightarrow a\gamma \rightarrow b\bar{b}\gamma)$ is the signal production cross-section, \mathcal{L} is the integrated luminosity, and ϵ is the signal efficiency. After repeating the analysis for each m_a , we obtain $\epsilon(m_a)$ and $N_B(m_a)$ as listed in Table 5. In Fig. 7, the 95% CL upper limit on $\sigma(pp \rightarrow a\gamma \rightarrow b\bar{b}\gamma)$ is shown as a function of ALP mass, by the solid blue line in the absence of systematic uncertainty, and by the (smaller) dashed blue line in the case of a 2% (5%) systematic uncertainty⁴. The limits are shown for $\sqrt{s} = 13$ TeV and $\mathcal{L} = 300 \text{ fb}^{-1}$, in the left panel of Fig. 7, and for $\sqrt{s} = 14$ TeV and $\mathcal{L} = 3000 \text{ fb}^{-1}$, in the right panel of Fig. 7. In the latter case, the upper limits are stronger and vary between $6.5 \cdot 10^4$ pb for an ALP mass of 12 GeV, and 119 pb for an ALP mass of 100 GeV. The limits weaken to $1.1 \cdot 10^5$ pb ($2.2 \cdot 10^5$ pb) and 237 pb (524 pb) upon adding 2% (5%) systematic uncertainty, respectively.

The limits are compared to the predicted cross-sections in the current ALP model, for different values of g_{aff} , as shown by the gray lines in Fig. 7. This shows that the HL-LHC will be sensitive to couplings in the range $g_{\text{aff}} \sim (0.05 - 0.1) \text{ GeV}^{-1}$, for an ALP mass in the range $m_a \sim (20 - 100) \text{ GeV}$. The sensitivity around the lowest mass value considered in this work, *i.e.* $m_a = 12$ GeV, is significantly weaker. In the next subsection, we will discuss the possibility to improve this sensitivity with modified trigger requirements. We also compare our bounds with the upper limits presented in Ref. [20] on $\sigma(pp \rightarrow Z'\gamma \rightarrow q\bar{q}\gamma)$, where the analysis is performed without flavour tagging. As a result of including flavour tagging, our bounds are significantly stronger in comparison.

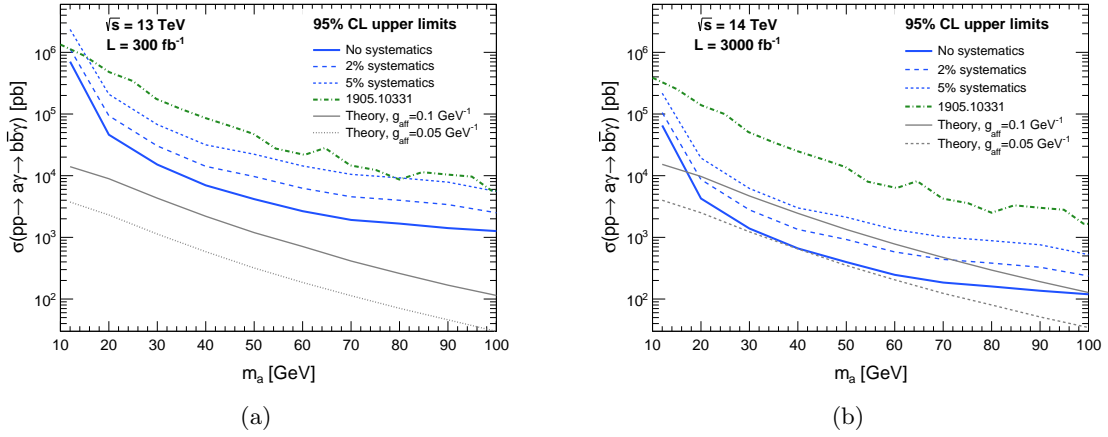


Figure 7: Upper limit at 95% C.L. on $\sigma(pp \rightarrow a\gamma \rightarrow b\bar{b}\gamma)$, as a function of the ALP mass. The limits are shown for (a) $\sqrt{s} = 13$ TeV with $\mathcal{L} = 300$ fb $^{-1}$ and (b) $\sqrt{s} = 14$ TeV with $\mathcal{L} = 3000$ fb $^{-1}$. The solid and (shorter) dashed blue lines correspond to neglecting systematic uncertainties or including them at the 2% (5%) level, respectively. The solid and dashed gray lines correspond to the theoretical prediction for the cross-section in the ALP model with $g_{\text{aff}} = 0.1$ GeV $^{-1}$ and 0.05 GeV $^{-1}$, respectively. For comparison, the dashed green line corresponds to the projected upper limit on the cross-section for an analogous process, $\sigma(pp \rightarrow Z'\gamma \rightarrow q\bar{q}\gamma)$ from Ref. [20].

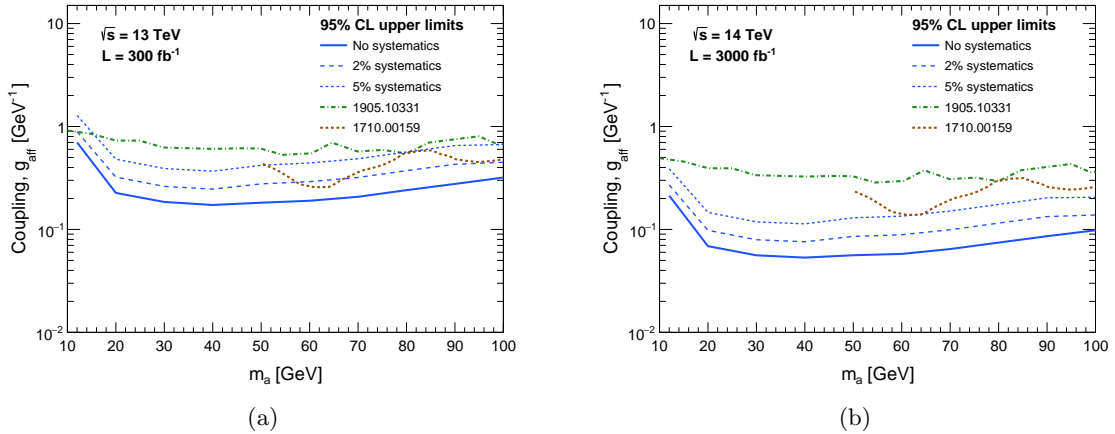


Figure 8: Upper limit at 95% C.L. on the ALP-fermion coupling g_{aff} , as a function of the ALP mass. The limits are shown for (a) $\sqrt{s} = 13$ TeV with $\mathcal{L} = 300$ fb $^{-1}$ and (b) $\sqrt{s} = 14$ TeV with $\mathcal{L} = 3000$ fb $^{-1}$. The solid and (shorter) dashed blue lines correspond to neglecting systematic uncertainties or including them at the 2% (5%) level, respectively. The dashed green and brown lines correspond to the projected upper limits from Ref. [20] and Ref. [39], respectively.

The derived upper limits on the signal production cross-section are translated into upper limits on the ALP-fermion coupling g_{aff} , as illustrated as a function of m_a in Fig. 8. The left and right panel corresponds to upper limits at $\sqrt{s} = 13$ TeV with $\mathcal{L} = 300 \text{ fb}^{-1}$ and $\sqrt{s} = 14$ TeV with $\mathcal{L} = 3000 \text{ fb}^{-1}$, respectively. The couplings above the blue solid and (shorter) dashed line can be excluded at 95% C.L. assuming zero or 2% (5%) systematic uncertainty, respectively. We observe that the stronger upper limit is obtained for an ALP mass $m_a \simeq 40$ GeV, with $g_{\text{aff}} \leq 0.053 \text{ GeV}^{-1}$ at $\sqrt{s} = 14$ TeV with $\mathcal{L} = 3000 \text{ fb}^{-1}$. For larger masses the limit slightly weakens, varying between $g_{\text{aff}} \lesssim (0.056 - 0.098) \text{ GeV}^{-1}$ in the range $m_a \sim (50 - 100)$ GeV. Adding 2% and 5% systematic uncertainty, the coupling reach degrades to $g_{\text{aff}} \lesssim (0.076 - 0.27) \text{ GeV}^{-1}$ and $(0.11 - 0.39) \text{ GeV}^{-1}$, respectively, in the ALP mass range between 10 GeV and 100 GeV. We compare these limits with the results available at the current LHC run at $\sqrt{s} = 13$ TeV with $\mathcal{L} = 35.9 \text{ fb}^{-1}$: the dashed green and brown lines are the projected 95% C.L. upper limits on the coupling to SM quarks, in the searches for a Z' resonance in association with a photon [20] or a jet [39], respectively. We observe that our limits are stronger as compared to these references, where the analyses were performed without any flavour decomposition of the jet.

4.2 Analysis with low p_T threshold

In the analysis presented earlier, we have adopted a $p_{T,\gamma} > 160$ GeV threshold for the triggered photon, consistently with what is currently done by ATLAS [21], discussed at the beginning of Section 3.2. In what follows, we assess the impact on the expected sensitivity of lowering the photon threshold to $p_{T,\gamma} > 100$ GeV, by repeating the analysis described in Section 3 with looser requirements on the AK1.0 jet transverse momentum, i.e. $p_T = 100$ GeV. The 95% C.L. upper limits on the ALP production cross-section, $\sigma(pp \rightarrow a\gamma \rightarrow b\bar{b}\gamma)$, and the ALP-fermion coupling, g_{aff} are shown in Fig. 9 and compared with the limits derived using the photon $p_{T,\gamma} > 160$ GeV and $p_{T,\text{AK1.0}} > 200$ GeV trigger strategy.

By loosening the requirement on the photon transverse momentum to $p_{T,\gamma} > 100$ GeV, the cross-section, $\sigma(pp \rightarrow a\gamma \rightarrow b\bar{b}\gamma)$ limits improve by a factor four at $m_a = 12$ GeV, varying between $1.6 \cdot 10^4$ pb and 146 pb for m_a between 12 and 70 GeV (above ~ 70 GeV, the sensitivity remains similar to the previous selection, $p_{T,\gamma} > 160$ GeV). The ALP-fermion coupling can be probed down to $g_{\text{aff}} \simeq 0.105 \text{ GeV}^{-1}$ at $m_a = 12$ GeV, while the maximal sensitivity, $g_{\text{aff}} \simeq 0.026 \text{ GeV}^{-1}$ is reached for $m_a \simeq 30 - 40$ GeV, although a slightly weaker bound is obtained $\simeq 0.057 \text{ GeV}^{-1}$ for $m_a \simeq 70$ GeV. Thus we find that the sensitivity to low-mass ALPs can be improved significantly with a stronger trigger requirement, in particular by lowering the p_T threshold for the accompanying photon.

4.3 Interpretation of the results

In order to assess the potential impact of these limits, it is interesting to visualise them along with existing constraints on the ALP parameter space. These existing constraints include limits from astrophysics and colliders which are summarised in Fig. 10, taken from Ref. [10].⁵ More precisely, the $m_a - g_{\text{aff}}$ parameter space is constrained by: astrophysical

⁴Adding $x\%$ systematic uncertainty, the signal significance formula is $S/\sqrt{N_B + (x \times N_B/100)^2}$.

⁵We are very grateful to Sophie Mutzel for providing the data required to reproduce these constraints.

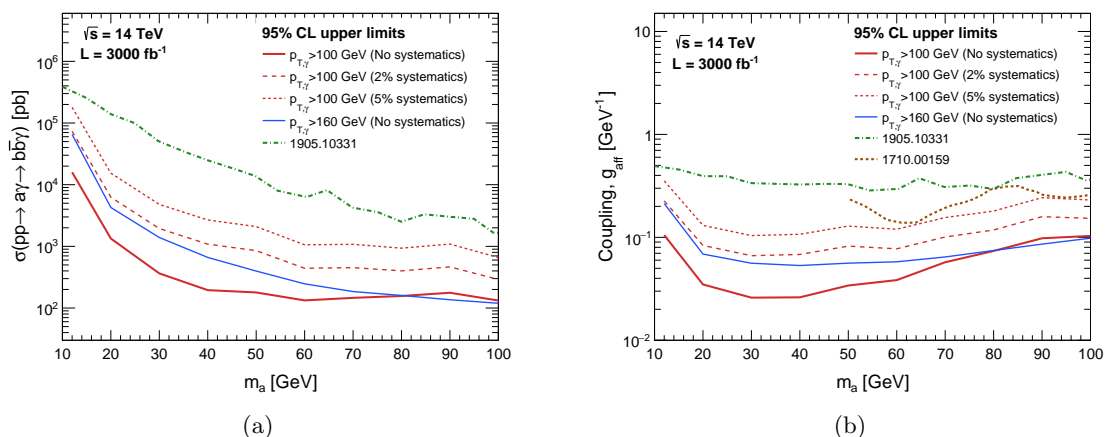


Figure 9: Upper limit at 95% C.L. on (a) $\sigma(pp \rightarrow a\gamma \rightarrow b\bar{b}\gamma)$ and (b) g_{aff} , with the requirement $p_{T,\gamma} > 100$ GeV, as a function of the ALP mass. The limits are shown for $\sqrt{s} = 14$ TeV with $\mathcal{L} = 3000$ fb $^{-1}$. Conventions are the same as in Fig. 7 and Fig. 8. The limit using the earlier selection, $p_{T,\gamma} > 160$ GeV, is shown with blue solid line.

constraints from SN1987A [62, 63] and Horizontal Branch (HB) stars [64, 65], excluding regions below $m_a \lesssim 100$ MeV and ~ 100 keV, respectively; collider constraints excluding regions above $g_{\text{aff}} \sim 10^{-5}$ GeV $^{-1}$ for ALP masses below 10 GeV, which include electron beam dump experiments from SLAC E137 [66] and heavy meson decays coming from LHCb, CHARM, NA62, NA48 [67–72]. Importantly, these bounds only apply below $m_a = 10$ GeV, whereas our derived projected limits constrain the ALP mass range between 12 GeV and 100 GeV. In Fig. 10, the dashed-dot blue line corresponds to the upper limit at $\sqrt{s} = 13$ TeV with $\mathcal{L} = 300$ fb $^{-1}$. While the dashed blue and red lines represent projections for $p_{T,\gamma} > 160$ GeV and 100 GeV, respectively, at $\sqrt{s} = 14$ TeV with $\mathcal{L} = 3000$ fb $^{-1}$. Projections for the LHC at $\sqrt{s} = 14$ TeV with $\mathcal{L} = 3000$ fb $^{-1}$ show that searches for the $b\bar{b}\gamma$ final state can probe the unexplored ALP mass regions ($\mathcal{O}(10)$ GeV) with a maximum reach of $g_{\text{aff}} \sim 0.026$ GeV $^{-1}$ under improved trigger requirements, $p_{T,\gamma} > 100$ GeV.

We note that since Ref. [10] appeared, direct constraints on ALP-fermion couplings have been further investigated. In Ref. [73] the authors studied a scenario in which the only non-zero coupling of the ALP to SM fermions was that to top quarks, *i.e.* $g_{\text{att}} \neq 0$ only. This has the important consequence that the ALP is long-lived with respect to the scale of the LHC detectors. As this is not the case in our model, the derived direct bounds do not apply here. Note that indirect bounds from the LHC on the ALP-top coupling were also derived in Ref. [73], and from low-energy, Higgs and top data to constrain the ALP-fermion couplings in Ref. [27]. In the former, indirect effects of the ALP on top pair production and gauge boson pair production are used to obtain limits on the ALP-top coupling. In the latter, bounds on the ALP couplings to up-type quarks (C_u), down-type quarks (C_d) and charged leptons (C_e) were obtained by taking into account renormalization group flow of these couplings into the SM effective field theory (SMEFT) Wilson coefficients, on

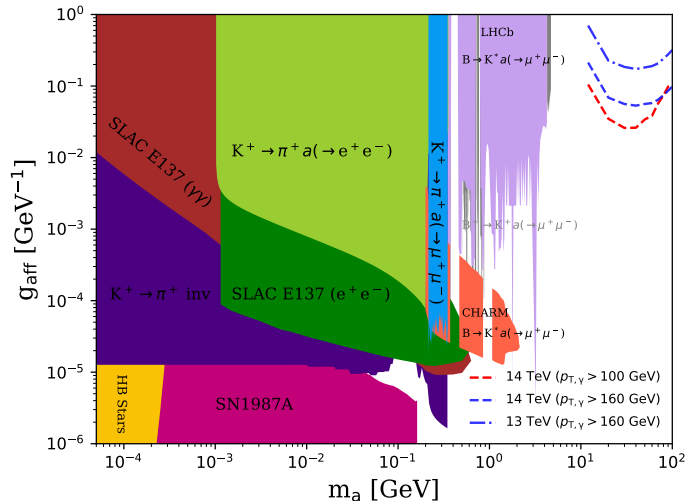


Figure 10: Constraints from astrophysical and collider experiments [10] together with our derived bounds on the ALP-fermion coupling, g_{aff} as a function of the ALP mass, m_a . The LHC bounds for $p_{T,\gamma} > 160$ GeV is shown with dashed-dotted and dashed blue color for $\sqrt{s} = 13$ TeV with $\mathcal{L} = 300 \text{ fb}^{-1}$ and $\sqrt{s} = 14$ TeV with $\mathcal{L} = 3000 \text{ fb}^{-1}$, respectively. The improvement with $p_{T,\gamma} > 100$ GeV requirement is shown with red dashed line at $\sqrt{s} = 14$ TeV with $\mathcal{L} = 3000 \text{ fb}^{-1}$.

which the constraints were already known. It turns out that particularly strong bounds on C_u/f_a were obtained, stemming from the two-loop contribution of the ALP-top coupling to the W mass. We note that not only do our direct constraints provide complementary information to these indirect bounds, they in addition provide the first direct constraints on the coupling of the ALP to down-type quarks in this region of m_a .

5 Summary and outlook

We have studied the LHC prospects for an ALP, a light pseudoscalar which primarily decays to a $b\bar{b}$ final state, in the mass range between 10 and 100 GeV. We considered a simple DFSZ-inspired scenario where the ALP only couples to SM fermions and this coupling is proportional to the fermion Yukawa.

To enhance the sensitivity to low ALP masses, we required a recoiling, high transverse-momentum photon. Since the ALP is boosted, we employed a larger radius jet with $R = 1.0$, to effectively capture the majority of the hadronisation products resulting from the decay of the ALP. Jet substructure techniques are implemented on the AK1.0 jet to reduce the multijet background. In this context, we utilised a two prong discriminant, N_2 , to identify the two prong structure in the signal AK1.0 jet, which originates from the $b\bar{b}$ final state. To reduce the p_T dependence of this observable, we modified it to a DDT observable, N_2^{DDT} . However, the efficacy of this observable weakens for very low ALP

masses, where the hadronisation products from the final state b -quarks merge and feature 1-prong substructure.

A crucial aspect in our analysis involves the b -tagging of the AK1.0 jet. We performed it by constructing at least two variable radius subjects inside the AK1.0 jet and matched them to a hadron in the event, resulting in 6 possible di-flavour combinations for the multijet background: bb , bc , bl , cc , cl , and ll . Standard tagging efficiencies for single-jet flavour can not be applied here. We included the corresponding tagging efficiencies for the signal and multijet rejection to those di-flavour combinations for the background provided by the ATLAS collaboration [50].

The final signal efficiency and background yields are calculated by performing a Crystal Ball fit to the signal m_{SD} distribution, and selecting the 1σ window around the fitted mean value. The upper limits are set at 95% confidence level on the $b\bar{b}\gamma$ production cross-section, $\sigma(pp \rightarrow a\gamma \rightarrow b\bar{b}\gamma)$. The HL-LHC limits vary between 185 pb and $4 \cdot 10^3$ pb, without systematics, 440 (1014) pb and $8.7 \cdot 10^3$ ($1.9 \cdot 10^4$) pb, with 2% (5%) systematics, for ALP masses between 20 GeV and 70 GeV. Translating the cross-section limits to the ALP-fermion coupling, the upper bound on g_{aff} , in the ALP mass range between 20 GeV and 70 GeV, is (0.053 - 0.069) GeV^{-1} at 95% CL. The g_{aff} upper limits worsen upon adding systematic uncertainty, and the maximum obtainable reach is 0.076 (0.11) GeV^{-1} , around $m_a \sim 40$ GeV, upon adding 2% (5%) systematics.

Comparing these limits to the existing LHC searches at the current run, we find that our analysis provides significantly better exclusion limits on the $b\bar{b}\gamma$ production cross-section. In addition, we complement our analysis with a reduced $p_{\text{T},\gamma}$ threshold, to assess the capability of our analysis in increasing the sensitivity to low mass scenarios. Indeed, our study demonstrates that the sensitivity to the cross-section improves by a factor of four at $m_a = 12$ GeV. The coupling g_{aff} can be excluded above 0.026 GeV^{-1} at 95% CL for $m_a \sim 30 - 40$ GeV. Thus, LHC searches on the proposed $b\bar{b}\gamma$ final state have sensitivity to the considered mass range which has not been explored yet by other complementary collider searches.

The analysis strategy presented can be readily applied to any well-motivated low mass resonance decaying into $b\bar{b}$. We also demonstrated the improvement in sensitivity obtained by lowering the trigger thresholds. Moreover, analyses using machine learning techniques could further improve the reach over the traditional observables with jet substructure techniques. Future lepton colliders may also enhance the low mass resonance search prospects, as we plan to explore in future work.

Acknowledgments

We would like to thank Sophie Mutzel, Yann Coadou, Andreas Goudelis, Amandip De for helpful discussions, and Carlos Carranza for computing support, during the course of this work. MF wishes to thank the laboratories CPPM and CPT for hospitality during the completion of this work. AA received support from the French government under the France 2030 investment plan, as part of the Initiative d'Excellence d'Aix-Marseille Université - A*MIDEX. MF received support from the European Union Horizon 2020 research

and innovation program under the Marie Skłodowska-Curie grant agreements No 860881-HIDDeN and No 101086085-ASYMMETRY. This work received support from the French government under the France 2030 investment plan, as part of the Excellence Initiative of Aix Marseille University - amidex (AMX-19-IET-008 - IPhU)

References

- [1] J. Jaeckel and A. Ringwald, *The Low-Energy Frontier of Particle Physics*, *Ann. Rev. Nucl. Part. Sci.* **60** (2010) 405 [[1002.0329](#)].
- [2] L. Di Luzio, M. Giannotti, E. Nardi and L. Visinelli, *The landscape of QCD axion models*, *Phys. Rept.* **870** (2020) 1 [[2003.01100](#)].
- [3] I. Brivio, M.B. Gavela, L. Merlo, K. Mimasu, J.M. No, R. del Rey et al., *ALPs Effective Field Theory and Collider Signatures*, *Eur. Phys. J. C* **77** (2017) 572 [[1701.05379](#)].
- [4] M. Bauer, M. Neubert and A. Thamm, *Collider Probes of Axion-Like Particles*, *JHEP* **12** (2017) 044 [[1708.00443](#)].
- [5] PARTICLE DATA GROUP collaboration, *Review of particle physics*, *Phys. Rev. D* **110** (2024) 030001.
- [6] X. Chu, T. Hambye and M.H. Tytgat, *The four basic ways of creating dark matter through a portal*, *Journal of Cosmology and Astroparticle Physics* **2012** (2012) 034.
- [7] C. Boehm, M.J. Dolan, C. McCabe, M. Spannowsky and C.J. Wallace, *Extended gamma-ray emission from Coy Dark Matter*, *JCAP* **05** (2014) 009 [[1401.6458](#)].
- [8] C. Arina, E. Del Nobile and P. Panci, *Dark Matter with Pseudoscalar-Mediated Interactions Explains the DAMA Signal and the Galactic Center Excess*, *Phys. Rev. Lett.* **114** (2015) 011301 [[1406.5542](#)].
- [9] T. Hambye, M.H.G. Tytgat, J. Vandecasteele and L. Vanderheyden, *Dark matter from dark photons: a taxonomy of dark matter production*, *Phys. Rev. D* **100** (2019) 095018 [[1908.09864](#)].
- [10] A. Bharucha, F. Brümmer, N. Desai and S. Mutzel, *Axion-like particles as mediators for dark matter: beyond freeze-out*, *JHEP* **02** (2023) 141 [[2209.03932](#)].
- [11] U. Ellwanger, C. Hugonie and A.M. Teixeira, *The Next-to-Minimal Supersymmetric Standard Model*, *Phys. Rept.* **496** (2010) 1 [[0910.1785](#)].
- [12] B. Gripaios, A. Pomarol, F. Riva and J. Serra, *Beyond the Minimal Composite Higgs Model*, *JHEP* **04** (2009) 070 [[0902.1483](#)].
- [13] M. Frigerio, A. Pomarol, F. Riva and A. Urbano, *Composite Scalar Dark Matter*, *JHEP* **07** (2012) 015 [[1204.2808](#)].
- [14] G. Cacciapaglia, G. Ferretti, T. Flacke and H. Serôdio, *Light scalars in composite Higgs models*, *Front. in Phys.* **7** (2019) 22 [[1902.06890](#)].
- [15] D. Buarque Franzosi, G. Cacciapaglia, X. Cid Vidal, G. Ferretti, T. Flacke and C. Vázquez Sierra, *Exploring new possibilities to discover a light pseudo-scalar at LHCb*, *Eur. Phys. J. C* **82** (2022) 3 [[2106.12615](#)].
- [16] D. Elander, M. Frigerio, M. Knecht and J.-L. Kneur, *Holographic models of composite Higgs in the Veneziano limit. Part I. Bosonic sector*, *JHEP* **03** (2021) 182 [[2011.03003](#)].

- [17] ATLAS collaboration, *Search for low-mass dijet resonances using trigger-level jets with the ATLAS detector in pp collisions at $\sqrt{s} = 13$ TeV*, *Phys. Rev. Lett.* **121** (2018) 081801 [[1804.03496](#)].
- [18] CMS collaboration, *Search for low mass vector resonances decaying into quark-antiquark pairs in proton-proton collisions at $\sqrt{s} = 13$ TeV*, *Phys. Rev. D* **100** (2019) 112007 [[1909.04114](#)].
- [19] M. Cacciari, G.P. Salam and G. Soyez, *The anti- k_t jet clustering algorithm*, *JHEP* **04** (2008) 063 [[0802.1189](#)].
- [20] CMS collaboration, *Search for Low-Mass Quark-Antiquark Resonances Produced in Association with a Photon at $\sqrt{s} = 13$ TeV*, *Phys. Rev. Lett.* **123** (2019) 231803 [[1905.10331](#)].
- [21] ATLAS collaboration, *Search for light resonances decaying to boosted quark pairs and produced in association with a photon or a jet in proton-proton collisions at $\sqrt{s} = 13$ TeV with the ATLAS detector*, *Phys. Lett. B* **788** (2019) 316 [[1801.08769](#)].
- [22] ATLAS collaboration, *Search for low-mass resonances decaying into two jets and produced in association with a photon using pp collisions at $\sqrt{s} = 13$ TeV with the ATLAS detector*, *Phys. Lett. B* **795** (2019) 56 [[1901.10917](#)].
- [23] CMS collaboration, *Search for low-mass resonances decaying into bottom quark-antiquark pairs in proton-proton collisions at $\sqrt{s} = 13$ TeV*, *Phys. Rev. D* **99** (2019) 012005 [[1810.11822](#)].
- [24] J. Quevillon and C. Smith, *Axions are blind to anomalies*, *Eur. Phys. J. C* **79** (2019) 822 [[1903.12559](#)].
- [25] M. Bauer, M. Neubert, S. Renner, M. Schnubel and A. Thamm, *The Low-Energy Effective Theory of Axions and ALPs*, *JHEP* **04** (2021) 063 [[2012.12272](#)].
- [26] F. Arias-Aragón, J. Quevillon and C. Smith, *Axion-like ALPs*, *JHEP* **03** (2023) 134 [[2211.04489](#)].
- [27] A. Biekötter, J. Fuentes-Martín, A.M. Galda and M. Neubert, *A global analysis of axion-like particle interactions using SMEFT fits*, *JHEP* **09** (2023) 120 [[2307.10372](#)].
- [28] D.K. Ghosh, A. Ghoshal and S. Jeessun, *Axion-like particle (ALP) portal freeze-in dark matter confronting ALP search experiments*, *JHEP* **01** (2024) 026 [[2305.09188](#)].
- [29] K. Nishijima, *Generalized Furry's Theorem for Closed Loops*, *Progress of Theoretical Physics* **6** (1951) 614.
- [30] J. Alwall, R. Frederix, S. Frixione, V. Hirschi, F. Maltoni, O. Mattelaer et al., *The automated computation of tree-level and next-to-leading order differential cross sections, and their matching to parton shower simulations*, *JHEP* **07** (2014) 079 [[1405.0301](#)].
- [31] T. Sjöstrand, S. Ask, J.R. Christiansen, R. Corke, N. Desai, P. Ilten et al., *An introduction to PYTHIA 8.2*, *Comput. Phys. Commun.* **191** (2015) 159 [[1410.3012](#)].
- [32] *ATLAS Pythia 8 tunes to 7 TeV data*, Tech. Rep. ATLAS-PHYS-PUB-2014-021, CERN, Geneva (2014).
- [33] NNPDF collaboration, *Parton distributions for the LHC Run II*, *JHEP* **04** (2015) 040 [[1410.8849](#)].
- [34] DELPHES 3 collaboration, *DELPHES 3, A modular framework for fast simulation of a generic collider experiment*, *JHEP* **02** (2014) 057 [[1307.6346](#)].

- [35] M. Cacciari, G.P. Salam and G. Soyez, *FastJet User Manual*, *Eur. Phys. J. C* **72** (2012) 1896 [[1111.6097](#)].
- [36] A.J. Larkoski, S. Marzani, G. Soyez and J. Thaler, *Soft Drop*, *JHEP* **05** (2014) 146 [[1402.2657](#)].
- [37] ATLAS collaboration, *Identification of hadronically-decaying top quarks using UFO jets with ATLAS in Run 2*, Tech. Rep. [ATL-PHYS-PUB-2021-028](#), CERN, Geneva (2021).
- [38] J. Dolen, P. Harris, S. Marzani, S. Rappoccio and N. Tran, *Thinking outside the ROCs: Designing Decorrelated Taggers (DDT) for jet substructure*, *JHEP* **05** (2016) 156 [[1603.00027](#)].
- [39] CMS collaboration, *Search for low mass vector resonances decaying into quark-antiquark pairs in proton-proton collisions at $\sqrt{s} = 13$ TeV*, *JHEP* **01** (2018) 097 [[1710.00159](#)].
- [40] I. Moult, L. Necib and J. Thaler, *New Angles on Energy Correlation Functions*, *JHEP* **12** (2016) 153 [[1609.07483](#)].
- [41] S.A. Dudani, *The distance-weighted k-nearest-neighbor rule*, *IEEE Transactions on Systems, Man, and Cybernetics* **SMC-6** (1976) 325.
- [42] ATLAS collaboration, *Optimisation and performance studies of the ATLAS b-tagging algorithms for the 2017-18 LHC run*, Tech. Rep. [ATL-PHYS-PUB-2017-013](#), CERN, Geneva (2017).
- [43] CMS collaboration, *Identification of heavy-flavour jets with the CMS detector in pp collisions at 13 TeV*, *JINST* **13** (2018) P05011 [[1712.07158](#)].
- [44] ATLAS collaboration, *ATLAS b-jet identification performance and efficiency measurement with $t\bar{t}$ events in pp collisions at $\sqrt{s} = 13$ TeV*, *Eur. Phys. J. C* **79** (2019) 970 [[1907.05120](#)].
- [45] ATLAS collaboration, *Boosted Higgs ($\rightarrow b\bar{b}$) Boson Identification with the ATLAS Detector at $\sqrt{s} = 13$ TeV*, Tech. Rep. [ATLAS-CONF-2016-039](#), CERN, Geneva (2016).
- [46] ATLAS collaboration, *Search for supersymmetry in events with b-tagged jets and missing transverse momentum in pp collisions at $\sqrt{s} = 13$ TeV with the ATLAS detector*, *JHEP* **11** (2017) 195 [[1708.09266](#)].
- [47] CMS collaboration, *Search for Supersymmetry in Final States with b Jets and Missing Energy at the LHC*, Tech. Rep. [CMS-PAS-SUS-10-011](#), CERN, Geneva (2011).
- [48] CMS collaboration, *Inclusive search for highly boosted Higgs bosons decaying to bottom quark-antiquark pairs in proton-proton collisions at $\sqrt{s} = 13$ TeV*, *JHEP* **12** (2020) 085 [[2006.13251](#)].
- [49] CMS collaboration, *Search for supersymmetry in the all-hadronic final state using top quark tagging in pp collisions at $\sqrt{s} = 13$ TeV*, *Phys. Rev. D* **96** (2017) 012004 [[1701.01954](#)].
- [50] ATLAS collaboration, *Transformer Neural Networks for Identifying Boosted Higgs Bosons decaying into $b\bar{b}$ and $c\bar{c}$ in ATLAS*, Tech. Rep. [ATL-PHYS-PUB-2023-021](#), CERN, Geneva (2023).
- [51] ATLAS collaboration, *Expected performance of the ATLAS b-tagging algorithms in Run-2*, Tech. Rep. [ATL-PHYS-PUB-2015-022](#), CERN, Geneva (2015).
- [52] CMS collaboration, *Identification of b-Quark Jets with the CMS Experiment*, *JINST* **8** (2013) P04013 [[1211.4462](#)].
- [53] D. Krohn, J. Thaler and L.-T. Wang, *Jets with Variable R*, *JHEP* **06** (2009) 059 [[0903.0392](#)].

- [54] ATLAS collaboration, *Variable Radius, Exclusive- k_T , and Center-of-Mass Subjet Reconstruction for Higgs($\rightarrow b\bar{b}$) Tagging in ATLAS*, Tech. Rep. [ATL-PHYS-PUB-2017-010](#), CERN, Geneva (2017).
- [55] S. Catani, Y. Dokshitzer, M. Seymour and B. Webber, *Longitudinally-invariant kt -clustering algorithms for hadron-hadron collisions*, *Nuclear Physics B* **406** (1993) 187.
- [56] M. Wobisch and T. Wengler, *Hadronization corrections to jet cross-sections in deep inelastic scattering*, in *Workshop on Monte Carlo Generators for HERA Physics (Plenary Starting Meeting)*, pp. 270–279, 4, 1998 [[hep-ph/9907280](#)].
- [57] ATLAS collaboration, *Identification of Boosted Higgs Bosons Decaying Into $b\bar{b}$ With Neural Networks and Variable Radius Subjets in ATLAS*, Tech. Rep. [ATL-PHYS-PUB-2020-019](#), CERN, Geneva (2020).
- [58] M. Oreglia, *A Study of the Reactions $\psi' \rightarrow \gamma\gamma\psi$* , other thesis, 12, 1980.
- [59] *Search for scalar diphoton resonances in the mass range 65-600 GeV with the ATLAS detector in pp collision data at $\sqrt{s} = 8$ TeV*, Tech. Rep. [ATLAS-CONF-2014-031](#), CERN, Geneva (2014).
- [60] G. Cowan, K. Cranmer, E. Gross and O. Vitells, *Asymptotic formulae for likelihood-based tests of new physics*, *Eur. Phys. J. C* **71** (2011) 1554 [[1007.1727](#)].
- [61] G. Cowan, *Discovery sensitivity for a counting experiment with background uncertainty*, tech. rep., Royal Holloway, London (2012), .
- [62] K.J. Kelly, S. Kumar and Z. Liu, *Heavy axion opportunities at the DUNE near detector*, *Phys. Rev. D* **103** (2021) 095002 [[2011.05995](#)].
- [63] F. Ertas and F. Kahlhoefer, *On the interplay between astrophysical and laboratory probes of MeV-scale axion-like particles*, *JHEP* **07** (2020) 050 [[2004.01193](#)].
- [64] M. Pospelov, A. Ritz and M.B. Voloshin, *Bosonic super-WIMPs as keV-scale dark matter*, *Phys. Rev. D* **78** (2008) 115012 [[0807.3279](#)].
- [65] F.T. Avignone, III, R.L. Brodzinski, S. Dimopoulos, G.D. Starkman, A.K. Drukier, D.N. Spergel et al., *Laboratory Limits on Solar Axions From an Ultralow Background Germanium Spectrometer*, *Phys. Rev. D* **35** (1987) 2752.
- [66] J.D. Bjorken, S. Ecklund, W.R. Nelson, A. Abashian, C. Church, B. Lu et al., *Search for Neutral Metastable Penetrating Particles Produced in the SLAC Beam Dump*, *Phys. Rev. D* **38** (1988) 3375.
- [67] LHCb collaboration, *Search for long-lived scalar particles in $B^+ \rightarrow K^+ \chi(\mu^+ \mu^-)$ decays*, *Phys. Rev. D* **95** (2017) 071101 [[1612.07818](#)].
- [68] LHCb collaboration, *Search for hidden-sector bosons in $B^0 \rightarrow K^{*0} \mu^+ \mu^-$ decays*, *Phys. Rev. Lett.* **115** (2015) 161802 [[1508.04094](#)].
- [69] B. Döbrich, F. Ertas, F. Kahlhoefer and T. Spadaro, *Model-independent bounds on light pseudoscalars from rare B-meson decays*, *Phys. Lett. B* **790** (2019) 537 [[1810.11336](#)].
- [70] NA62 collaboration, *Measurement of the very rare $K^+ \rightarrow \pi^+ \nu \bar{\nu}$ decay*, *JHEP* **06** (2021) 093 [[2103.15389](#)].
- [71] NA48/2 collaboration, *Precise measurement of the $K^{+-} \rightarrow \pi^{+-} e^+ e^-$ decay*, *Phys. Lett. B* **677** (2009) 246 [[0903.3130](#)].

- [72] NA48/2 collaboration, *Searches for lepton number violation and resonances in $K^\pm \rightarrow \pi\mu\mu$ decays*, *Phys. Lett. B* **769** (2017) 67 [[1612.04723](#)].
- [73] F. Esser, M. Madigan, V. Sanz and M. Ubiali, *On the coupling of axion-like particles to the top quark*, *JHEP* **09** (2023) 063 [[2303.17634](#)].